Impact of hydrogen combustion on the oxidation-induced degradation of heavy-duty diesel engine piston materials

R. Pillai
Oak Ridge National Laboratory
1, Bethel Valley Road
Oak Ridge, TN, 37831
USA

T. Lowe
Oak Ridge National Laboratory
1, Bethel Valley Road
Oak Ridge, TN, 37831
USA

J.A. Haynes
Oak Ridge National Laboratory
1, Bethel Valley Road
Oak Ridge, TN, 37831
USA

D.T. Pierce
Oak Ridge National Laboratory
1, Bethel Valley Road
Oak Ridge, TN, 37831
USA

ABSTRACT

High temperature ferritic-martensitic steels are candidate materials for heavy-duty diesel engine pistons. The envisioned transition to hydrogen blended fuels is expected to alter the post-combustion atmosphere in the engines, primarily resulting in a higher water vapor content (> 20 vol%) and potentially higher exhaust gas temperatures. The oxidation resistance of existing and newly developed alloys will be a critical life-limiting mechanism under these conditions. In the present work, the oxidation behavior of candidate piston alloys was evaluated in air+10 vol.% H_2O and air+30 vol.% H_2O at 700°C. Thermal cyclic (1h cycle) exposures were conducted for two variants of commercial UNSS42200 ferritic-martensitic steel and two developmental alloy steels for up to 300h. The developmental alloys each have similar compositions but with one containing elevated Cu levels of 3 wt.%, A significant reduction in resistance to breakaway oxidation was observed for the commercial alloys in the higher water vapor atmosphere. Microstructural characterization (optical metallography, scanning electron microscopy and electron microprobe analysis) revealed the formation of thick Fe-rich oxides even for the high Cr (~12 wt.%) steels after an initial stage of protective oxidation with MnCr-rich spinels. The impact of the evaporation-induced loss of Cr on the time and temperature dependent compositional changes in the alloys was correlated with experimental findings. For the developmental alloys, Cu additions appear to play a role in significantly reducing oxidation kinetics in air+30 vol.% H_2O at 700°C.

Key words: H_2-combustion, heavy-duty diesel engines, wet air oxidation, pistons

INTRODUCTION

Hydrogen is considered vital to a carbon-neutral energy landscape of the future which includes power generation technologies such as H_2-fueled turbines [1] and internal combustion engines (ICEs) for the

transportation sector [2]. A detailed review discusses the suitability of hydrogen as an alternative fuel for internal combustion engines in terms of improved performance [3]. The article highlighted critical drawbacks of H_2-fueled ICEs, including potentially high-NOx emissions and issues of engine durability and reliability. The use of H_2 as fuel will necessitate modifications to engine subsystems and components and potential materials related needs as mentioned in [3]. Furthermore, there is a continuous need to pursue efficiency improvements while concurrently meeting strict emissions criteria. Typically, this usually results in increased component (e.g., pistons) temperatures. Recent developments indicate that peak cylinder pressures and temperatures for heavy duty ICEs will be required to exceed 250 bar and 500°C respectively to further improve fuel economy and specific power output [4]. These conditions are beyond the operational limits of Fe-based alloys (e.g., UNS G41400 steel) presently used for key components such as pistons. One of the primary challenges to address is the high temperature corrosion resistance of existing materials employed for the engine components in the H_2 post-combustion environment, which is expected to contain > 20 vol.% H_2O compared to a maximum of 10 vol.%, typically observed in conventional diesel engines.

Water vapor in exhaust gas is known to significantly deteriorate the oxidation resistance of heat-resistant steels [5] and Ni-base alloys [6] compared to dry air. Elevated water vapor content is expected to further accelerate the oxidation-induced degradation of structural materials for heat engines by either hindering the formation or inducing evaporation [7] and spallation [8] of protective surface oxides such as chromia (Cr_2O_3) and alumina (Al_2O_3). The oxidation behavior of UNS G41400 steel is known to be significantly affected in air+10% H_2O at temperatures > 550°C [9]. Several high Cr-containing commercially available ferritic-martensitic (FM) steels, including UNSS42200, 403Cb+, and X22CrMoV12-1, are under evaluation to replace UNS G41400 in the crowns of heavy-duty diesel engine pistons [9, 10]. These high Cr containing steels generally demonstrated better oxidation behavior compared to UNS G41400 steel in 10% H_2O, even when accounting for the fact they may operate at significantly higher operating temperatures in pistons due to their lower thermal conductivity than UNS G41400 [9]. However, there is no data reporting the behavior of these materials in the higher H_2O-containing environments expected during H_2 combustion.

In the present work, the oxidation behavior of candidate alloys for heavy duty diesel engine pistons was evaluated in air+10 vol.% (designated as air+10% hereafter) H_2O and air+30 vol.% (designated as air+30% hereafter) H_2O at 700°C. Thermal cyclic (1h cycle) exposures were conducted for two variants of commercial UNSS42200 ferritic-martensitic (FM) steel for up to 300h in both environments and two developmental alloy steels in air+30%H_2O for up to 250h. The developmental alloys were selected based on ongoing research to develop novel alloys for heavy-duty diesel engine pistons. The chosen developmental alloy compositions consisted of additions of key alloying constituents such as C, N, Nb, V and Mo for evaluated temperature strengthening and Cr for oxidation resistance. In addition, elevated levels of Cu are uniquely leveraged in developmental alloy 1 (DA-1) to further enhance oxidation resistance while not adversely affecting thermal conductivity, since alloying induced reductions in thermal conductivity can increase piston operating temperature, potentially negating improvements in oxidation resistance. The composition of DA-2 is nominally the same as DA-1, except without Cu additions, and provided valuable comparisons of the impact of chemical composition on oxidation behavior to DA-1 and the UNSS42200 steel variants. Microstructural characterization (optical metallography, scanning electron microscopy and electron microprobe analysis) revealed the formation of thick Fe-rich oxides even for the high Cr (~12 wt.%) steels after an initial stage of protective oxidation with MnCr-rich spinels. The impact of the evaporation-induced loss of Cr on the time and temperature dependent compositional changes in the alloys was correlated with experimental findings. For brevity, the present work will primarily focus on the results of the exposures in air+30 vol.% H_2O while relevant experimental observations for the exposures in air+10 vol.% H_2O will be exclusively utilized to discuss and interpret key findings.

EXPERIMENTAL PROCEDURE

The UNSS42200 steel variants were procured as commercial round bar stock [9]. Alloys DA-1 and DA-2 were arc melted and cast to ingots of approximately 25.4 mm x 25.4 mm x 127 mm in length then hot

rolled. All alloys were austenitized, quenched, and tempered to form a tempered martensitic microstructure. Rectangular coupons (~10×20×1.5 mm^3) of the studied alloys were ground to a 600-grit finish and ultrasonically cleaned in acetone and methanol prior to exposure. The measured compositions of the alloys are given in Table 1. Samples were exposed in automated cyclic rigs [13] for 1h cycles at the 700°C) in flowing air+(10 ± 1) vol.% H_2O and air+(30 ± 1) vol.% H_2O (500 $cm^3.min^{-1}$ and 0.60-0.68 $cm.s^{-1}$ gas flow rate and velocity respectively) followed by 10 min. cooling in laboratory air after being automatically pulled out from the furnace. Three specimens of each alloy were tested and one of each alloy was taken out after desired times of 50, 100, and 300h respectively. Specimens mass changes were measured after every 20, 1h-cycles during the first 100 h and thereafter every 50, 1h cycles using a Mettler-Toledo model XP208 balance with an accuracy of ± 0.04 mg. After exposure the specimens were Cu electroplated, cross-sectioned and mounted. The mounted samples were polished using SiC papers, diamond pastes (1 micron) and colloidal SiO2 for cross-sectional characterization including scanning electron microscopy (SEM) using a TESCAN model MIRA3, energy dispersive X-ray spectroscopy (EDS) using an EDAX Octane Elect Super Silicon Drift Detector with an EDS detector (70 mm^2). EDS elemental mapping was performed at 20kV and quantitatively analyzed using the APEX EDS 3.0 software with the ZAF correction method (Z: atomic number, A: absorbance, F: fluorescence) and in-built standards.

Table 1: Measured composition in wt.% by direct current plasma emission spectroscopy, combustion analysis for carbon, and inert gas fusion for N.

Alloy	Fe	Cr	Ni	W	Mn	Mo	V	Si	Cu	Nb	C	N
UNSS42200-U	Bal.	11.3	0.8	1.1	0.7	1.0	0.25	0.32	0.09	0.006	0.21	0.06
UNSS42200-C	Bal.	11.9	0.8	1.1	0.8	1.1	0.22	0.44	0.08	0.01	0.23	0.05
DA-1	Bal.	11.3	1.0	0.03	0.27	0.5	0.26	0.36	2.97	0.31	0.08	0.09
DA-2	Bal.	10.9	1.0	0.06	0.26	0.5	0.26	0.37	0.003	0.32	0.08	0.01

RESULTS

Figure 1 compares the mass changes of UNSS42200-U (**Figure 1**a) and UNSS42200-C (**Figure 1**b) in air+10% H_2O and in air+30% H_2O at 700°C. The mass change for UNSS42200-U was comparable between the two atmospheres after only 50h except for one specimen exposed in air+10%H_2O which showed a significantly lower mass gain until 60h.

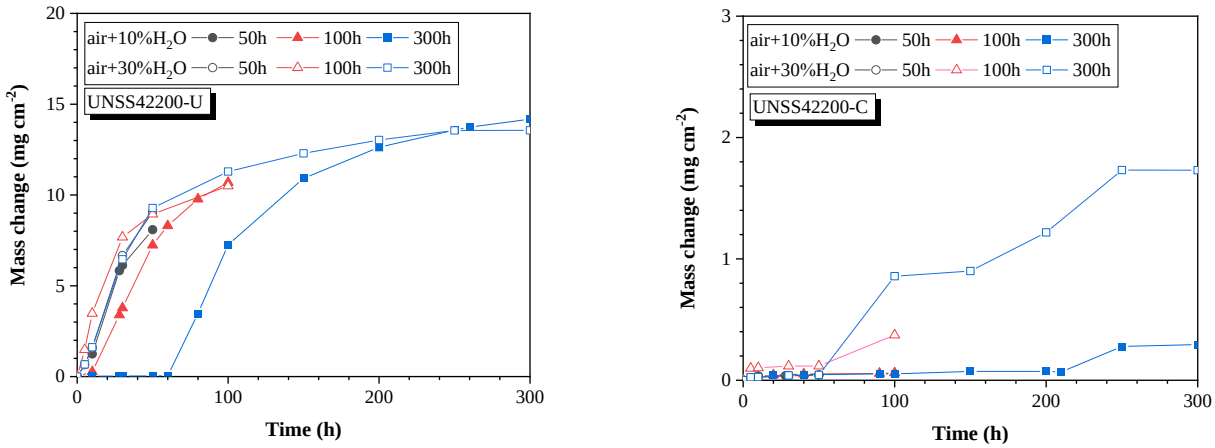

Figure 1: Measured mass change for (a) UNSS42200-U and (b) UNSS42200-C after exposure in air+10% H_2O and air+30% H_2O for 50, 100 and 300h at 700°C (1h-cycles). Note the different scales on the vertical axes of (a) and (b).

In the case of UNSS42200-C, higher mass gains were observed in the higher H_2O content. However, for UNSS42200-C, the mass change in air+30% H_2O started deviating from the values in air+10% H_2O between 50 and 100h. Total mass gains after 300h at the higher water vapor level were much lower for UNSS42200-C as compared to UNSS42200-U. The BSE images of cross-sections for UNSS42200-U after exposure in air+10% H_2O (**Figure 2**a and b) and in air+30% H_2O (**Figure 2**c and d) are shown after 50 and 100h at 700°C. In agreement with the mass change, exposures in both atmospheres have resulted in similar oxide morphologies with an outward growing Fe-rich oxide scale and an inward growing FeCr-rich mixed oxide. **Figure 3** shows the BSE images of the cross-sections of UNSS42200-C after exposure in the two atmospheres for 50 (**Figure 3**a and d), 100 (**Figure 3**b and e) and 300h (**Figure 3**c and f) at 700°C. The oxide morphologies and thicknesses between the two exposures were observed to be similar for the 50 and 100h exposures. However, the oxide scale was slightly thicker after 300h for the specimen exposed in air+30% H_2O.

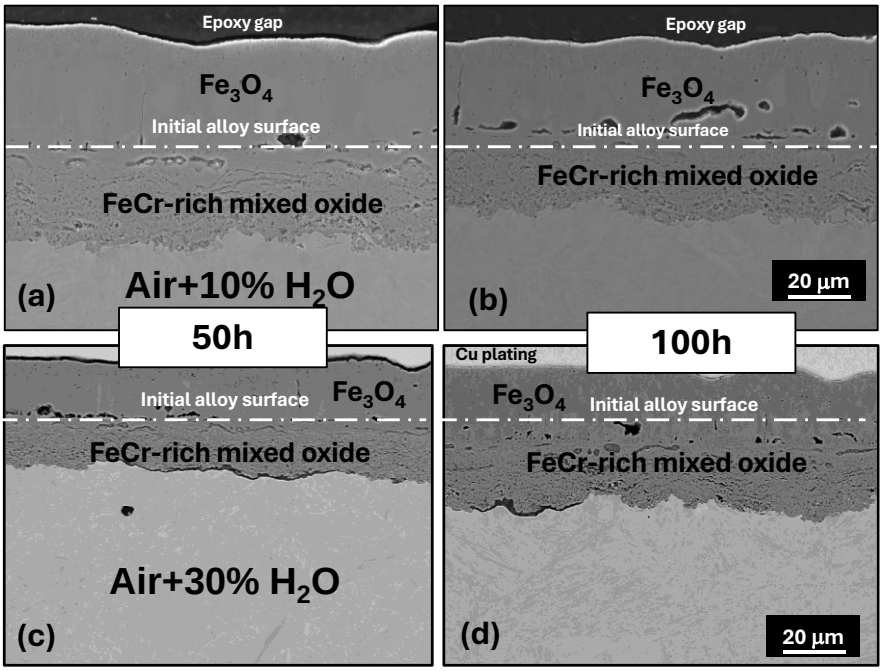

Figure 2: BSE images of the cross-sections of UNSS42200-U after exposure in (a), (b) air+10% H_2O and in (c), (d) air+30% H_2O for 50 and 100h at 700°C.

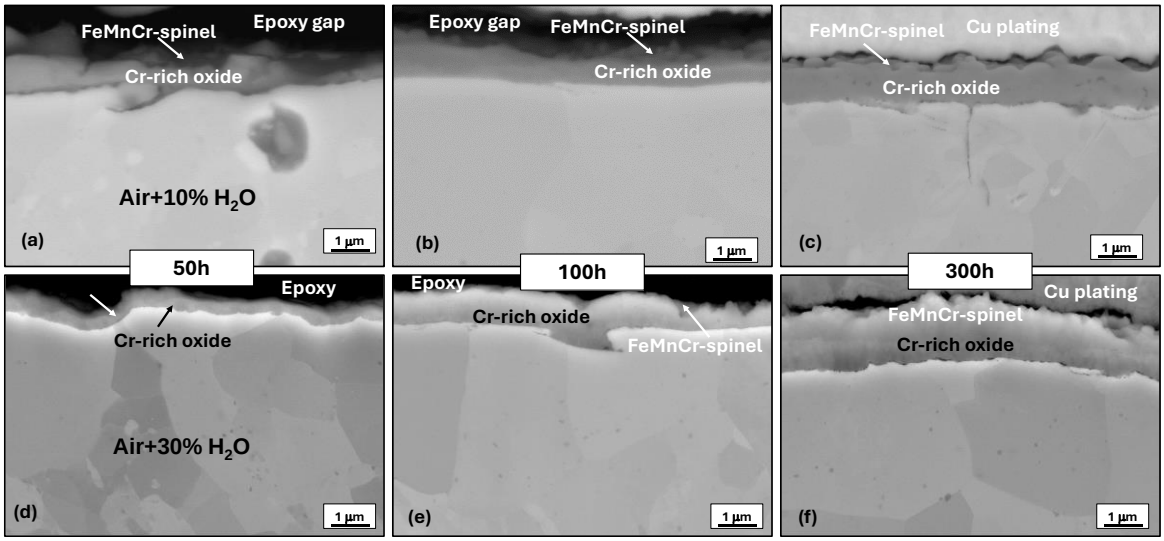

Figure 3: BSE images of the cross-sections of UNSS42200-C after exposure in (a), (b) and (c) air+10% H_2O and in (d), (e) and (f) air+30% H_2O for 50, 100 and 300h at 700°C.

The elemental distribution maps for UNSS42200-U after 50h in air+10%H_2O, shown in **Figure 4**, confirm the nature of the oxide scale as mentioned earlier. Similar distribution maps were observed (not shown here) for the specimen exposed in the higher H_2O-containing atmosphere. In case of UNSS42200-C, similar oxide scales were observed for exposures in the two atmospheres. Representative element distribution maps for the specimen exposed for 300h in air+10% H_2O are shown in **Figure 5**. The outer layer was observed to be a FeCrMn-rich spinel with a Cr-rich oxide underneath. The observation of similar oxide constitutions does not explain the higher mass gain observed for the specimen exposed for 300h in air+30% H_2O. A closer look at the specimen exposed in the higher H_2O-containing atmosphere revealed multiple locations with Fe-rich oxide surface nodules as shown in **Figure 6**. This suggests a faster breakdown of the oxide for UNSS42200-C in the higher H_2O-containing atmosphere.

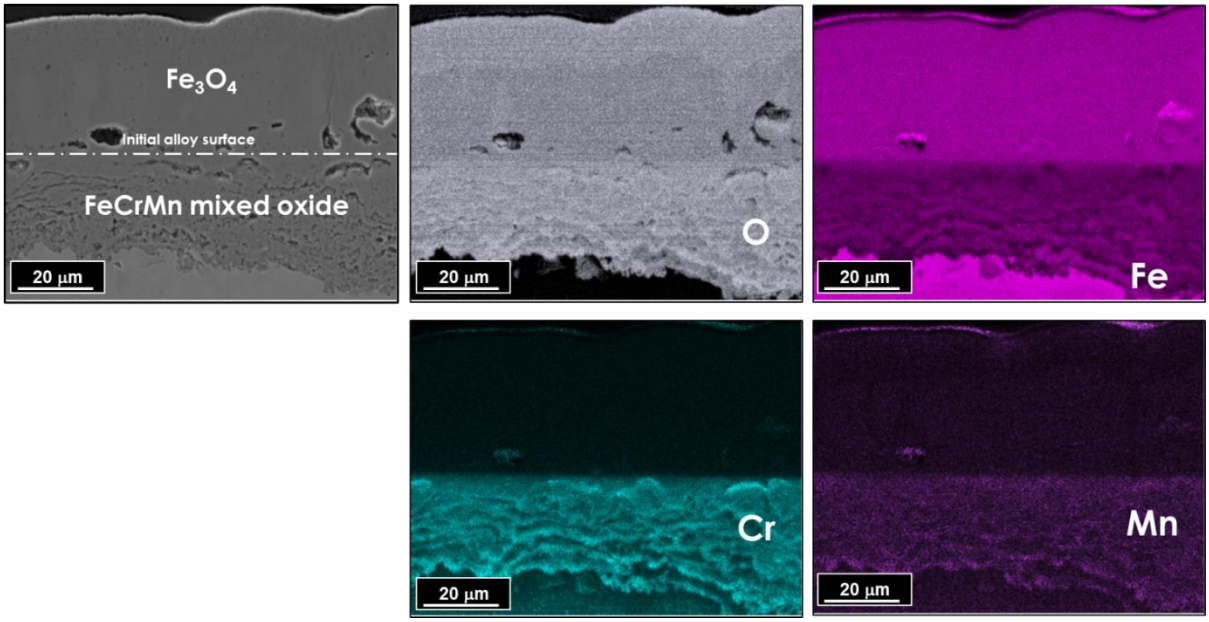

Figure 4: Elemental distribution maps of the cross-section of UNSS42200-U after exposure in air+10% H_2O for 50h at 700°C.

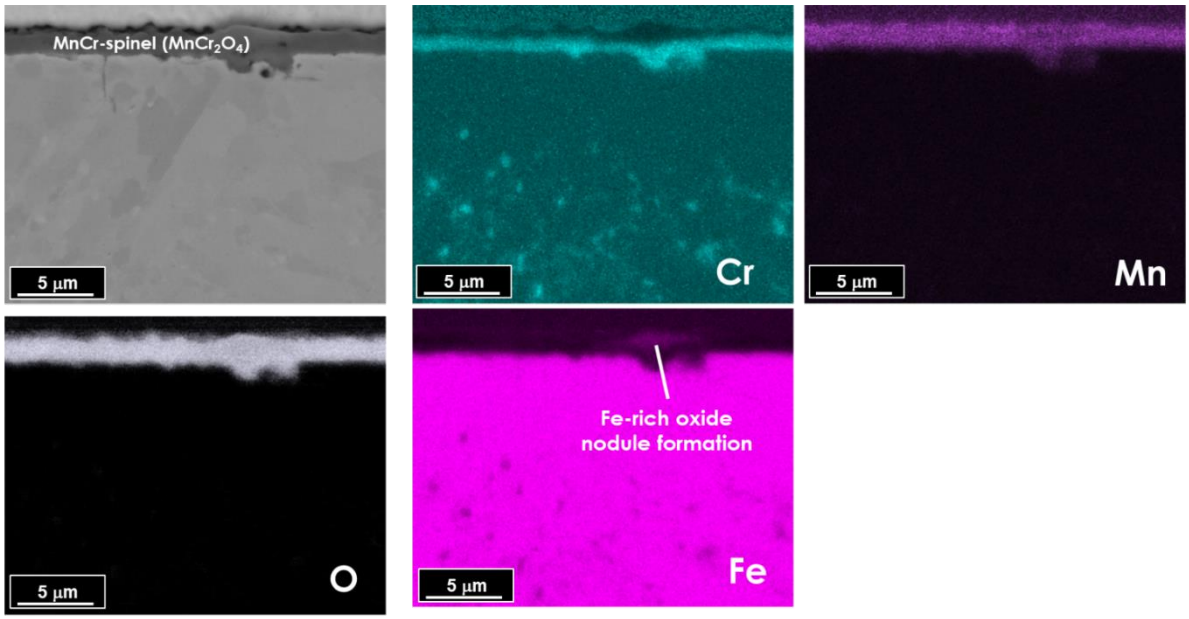

Figure 5: Elemental distribution maps of the cross-section of UNSS42200-C after exposure in air+10% H_2O for 50h at 700°C.

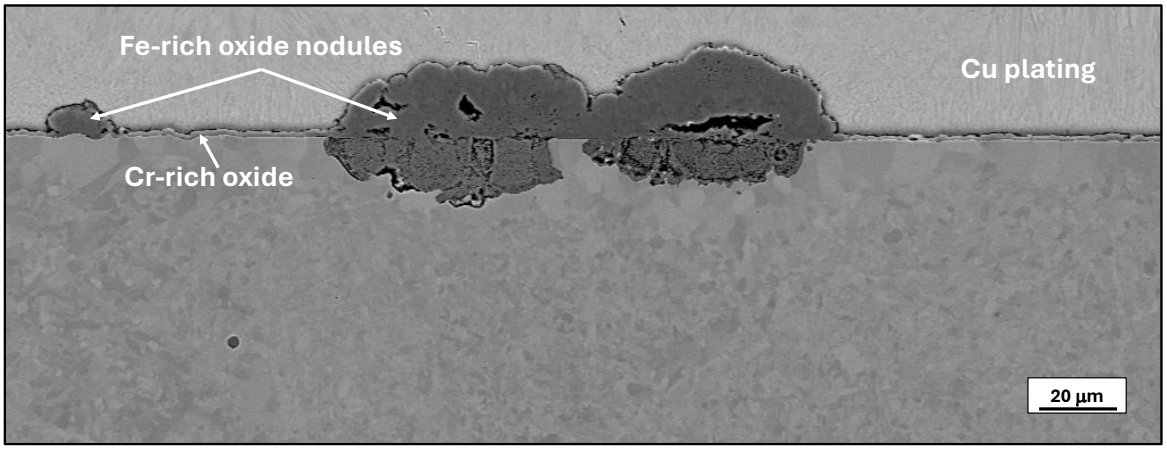

Figure 6: BSE images of the cross-sections of UNSS42200-C after exposure in air+30% H_2O for 300h at 700°C.

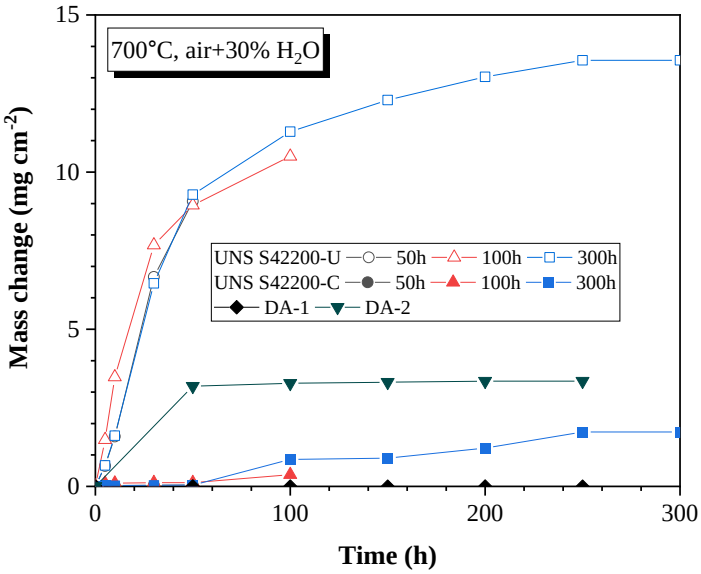

Figure 7: Measured mass change for UNSS42200-U, UNSS42200-C, DA-1 and DA-2 after exposure in air+30% H_2O for 50, 100 and 300h at 700°C.

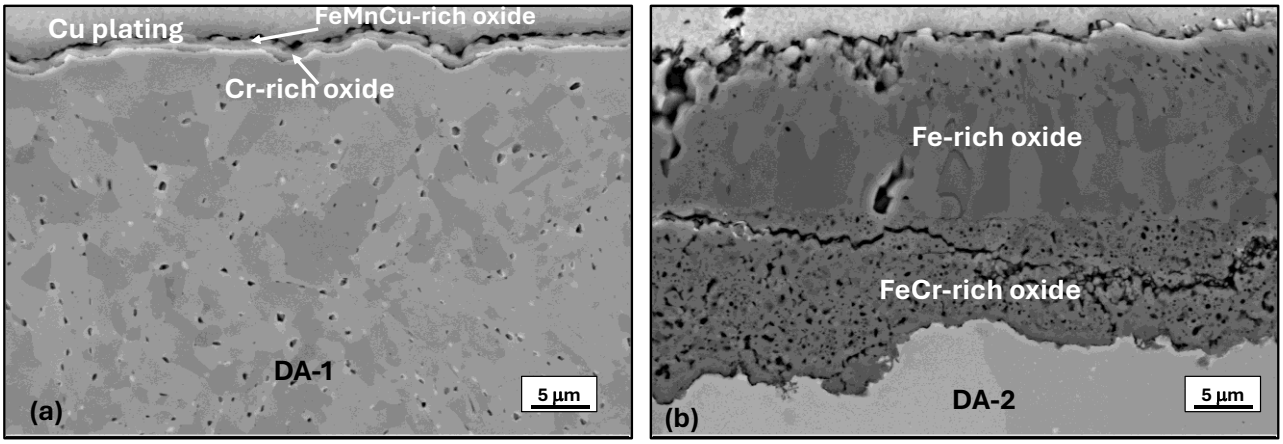

Figure 8: BSE images of the cross-sections of DA-1 and DA-2 after exposure in air+30% H_2O for 250h at 700°C.

Figure 7 compares the mass change of the developmental alloys DA-1 and DA-2 with UNSS42200-C and UNSS42200-U. Interestingly, DA-1 was observed to show negligible mass gain (within the error bar of the scale) while the mass gain for DA-2 was between UNSS42200-U and UNSS42200-C. The BSE images of the cross-sections of DA-1 and DA-2 after exposure in air+30% H_2O for 250h at 700°C (**Figure 8**a and b, respectively) agree with the mass change results. An extremely thin oxide scale was observed for DA-1 while a similar duplex scale to that observed for UNSS42200-U was also present on DA-2, although significantly thinner.

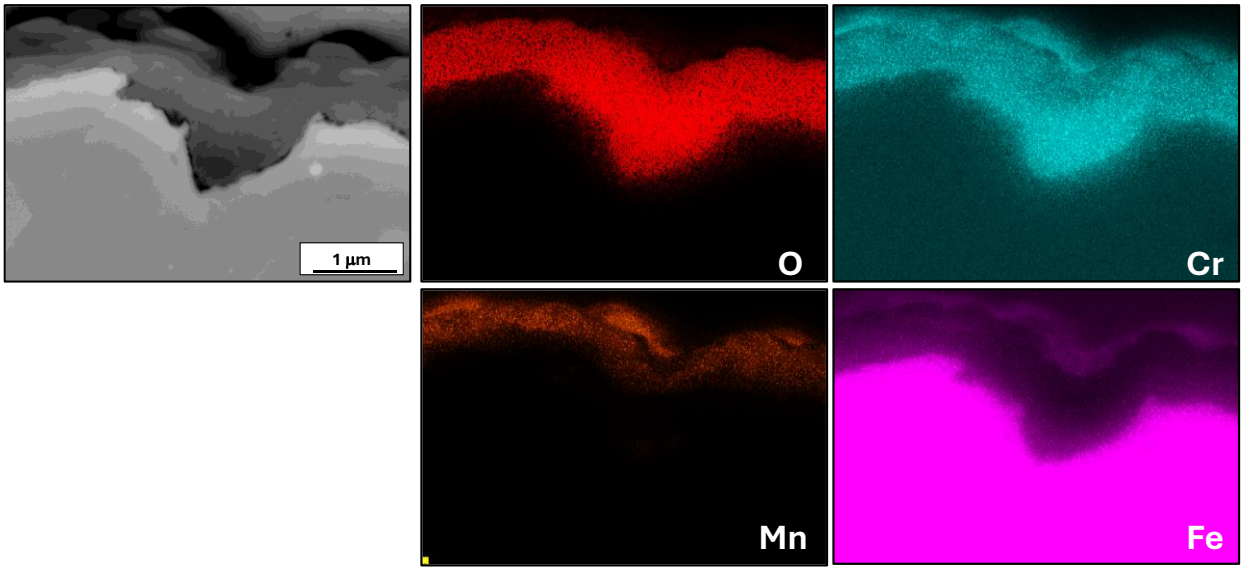

Figure 9: Elemental distribution maps of the cross-section of DA-1 after exposure in air+30% H_2O for 250h at 700°C

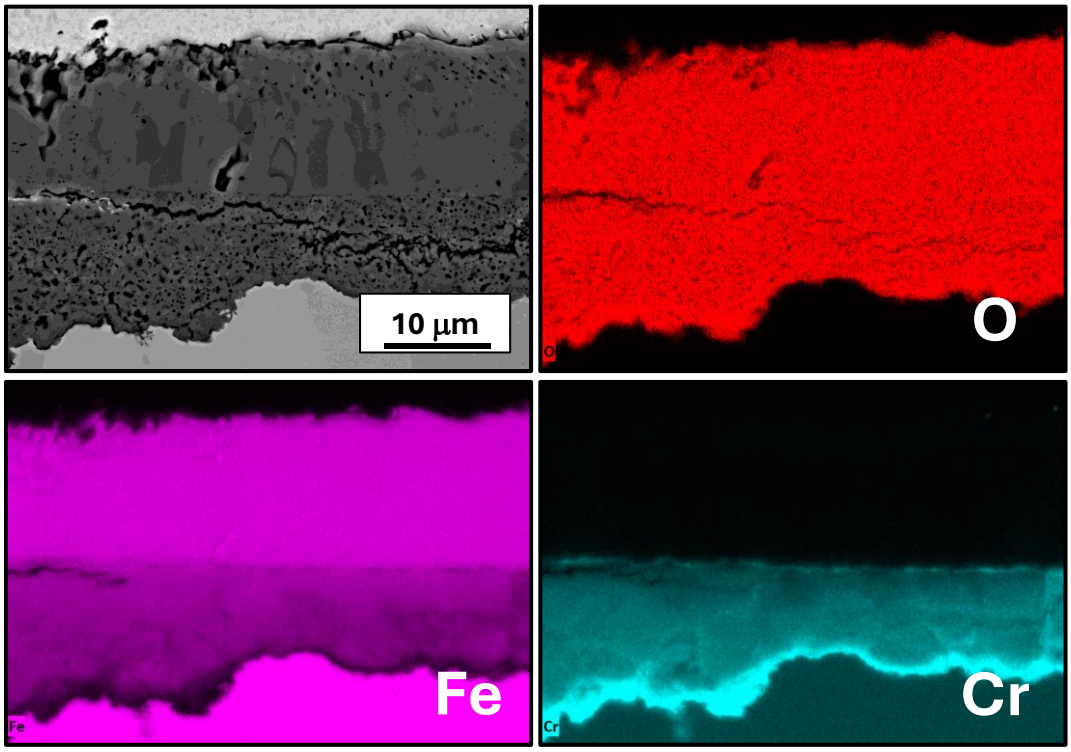

Figure 10: Elemental distribution maps of the cross-section of DA-2 after exposure in air+30% H_2O for 250h at 700°C.

The oxide scale constitution in case of DA-1 showed an outer FeCuMn-rich spinel (confirmed with EDS) with a Cr-rich oxide underneath (**Figure 9**). Element distribution maps for DA-2 (**Figure 10**) confirm the nature of the oxide layers with an outer Fe-rich oxide and inner FeCr-rich mixed oxide. The inner oxide shows significant porosity and there is indication of cracking at the interface between the outer and inner oxide layers.

DISCUSSION

Based on Wagner's theory [11], the minimum Cr content N_{Cr}^{1} required to form an external Cr_2O_3 scale can be calculated as,

$$N_{\mathrm{Cr}}^{1} = \sqrt{\frac{\pi f_{\mathrm{IOZ}}^{*}}{2\nu}\frac{V_{\mathrm{alloy}}}{V_{\mathrm{oxide}}}\frac{N_{\mathrm{O}}^{(s)} D_{\mathrm{O}}}{D_{\mathrm{Cr}}}} \qquad (1)$$

where V_{alloy} and V_{oxide} are the molar volumes of the alloy and oxide ($CrO_{1.5}$) respectively with B being the oxide-forming element (Cr) and f_{IOZ}^{*} is the critical volume fraction of internal oxides beyond which an external scale may form. Inputting the values given in Table *2*, the minimum Cr content required to form an external Cr_2O_3 scale was calculated to about 9.5 wt.%. The value of D_{Cr} was calculated from the data provided by Williams and Faulkner [12] for a Fe-12Cr steel while simultaneously accounting for grain boundary diffusion (assuming a 25 micron average grain size) [13], which can be expected to be a significant contributor to Cr transport, especially on the cold-worked surface due to specimen preparation.

Table 2: Parameters used to calculate minimum Cr required to form an external chromia scale

$N_{\mathrm{O}}^{(s)}$ [14]	D_{O} (cm^2/s) [14]	D_{Cr} (cm^2/s) [12]	V_{alloy} (cm^3/mol)	V_{oxide} (cm^3/mol)	f_{IOZ}^{*} [15]	ν
9.96×10^{-7}	4.5×10^{-8}	5.9×10^{-13}	6.8	14.6	0.3	1.5

The two FM-steels UNSS42200-U and UNSS42200-C with their Cr content > 11 wt.% are hence both expected to form protective chromia scales. However, Fe-rich oxides were observed on UNSS42200-U after 50h in both atmospheres, except for one specimen. The significantly low mass gain for this specimen suggests that a chromia scale did potentially form on UNSS42200-U, but the scale could not be sustained to 50h. However, a thin chromia scale was clearly sustained to 300 h in the case of UNSS42200-C. Wagner's second criteria provides some guidance in this regard by providing the following equation to estimate the minimum concentration required at the scale/alloy interface N_{Cr}^{2} to sustain external scale formation,

$$N_{\mathrm{Cr}}^{2} = \frac{V_{\mathrm{alloy}}}{V_{\mathrm{oxide}}}\sqrt{\frac{\pi k_{\mathrm{p}}}{2D_{\mathrm{Cr}}}} \qquad (2)$$

where k_{p} is the parabolic oxidation rate of the chromia scale. In the current atmosphere, evaporation of chromia in wet air to result in Cr-oxyhydroxides, which is a well-known phenomenon [16], will additionally accelerate depletion of Cr from the alloy [17]. This kinetics of this effect are known to be enhanced with increasing contents of H_2O [17]. Following the approach previously reported in the literature [7, 17], the evaporation rates of Cr were calculated in the two environments studied here by utilizing the thermodynamic data from Opila et al. The Cr loss rate due to evaporation of chromia was 1.3×10^{-7} g cm^{-2} h^{-1} in air+10% H_2O and 3.43×10^{-7} g cm^{-2} h^{-1} in air+30% H_2O. Thus, the Cr loss rate is about three times higher in the air+30% H_2O environment. Hence, it is not surprising that in case of UNSS42200-C, the chromia scale showed preliminary signs of breakaway in air+30% H_2O after 300h. All the experimental observations point toward the role of the slightly differing Cr contents in the two alloys as determining the observed differences in oxidation behavior.

The k_p for oxide growth was estimated from short-term experiments (5h and 10h) that were conducted in dry air (not shown here) and was calculated to be 1.5x10^{-14} g^2 cm^{-4} s^{-1} (5.3x10^{-15} cm^2 s^{-1}) to eliminate the impact of oxide evaporation on oxide growth. Limited short-term testing in air+10%H_2O (5h) resulted in similar values for k_p which suggested negligible impact of water vapor on oxide growth in this case. The calculated Cr loss due to evaporation can be converted to an equivalent oxide growth and was calculated to be 7.8x10^{-11} g cm^{-2} s^{-1} (1.5x10^{-11} cm s^{-1}) in air+10% H_2O and 2.1x10^{-10} g cm^{-2} s^{-1}(4x10^{-11} cm s^{-1}) in air+30% H_2O. Eq. 2 is derived assuming parabolic oxide growth but does not account for the additional evaporation-induced Cr loss. The flux of Cr at the oxide-alloy interface to support chromia growth J_{Cr} can be written as [18],

$$J_{Cr} = \sqrt{\frac{D}{\pi t}} \frac{N_{Cr,o} - N_{Cr,i}}{V_{alloy}} \tag{3}$$

Where $N_{Cr,o}$ and $N_{Cr,i}$ are the Cr concentrations in the bulk and at the oxide-alloy interface respectively and D is the interdiffusion coefficient of Cr in the alloy. The rate of Cr incorporation (as moles of Cr n_{Cr}) in the chromia scale can be equated to the Cr flux as

$$J_{Cr} = \frac{d\left(\frac{n_{Cr}}{A}\right)}{dt} \tag{4}$$

The amount of Cr incorporation is equivalent to the scale thickening rate X as

$$d\left(\frac{n_{Cr}}{A}\right) = d\left(\frac{X}{V_{\text{oxide}}}\right) \tag{5}$$

For parabolic oxidation kinetics X can be defined as $\sqrt{2k_p t}$ and Eq. 2 can be derived by combining Eqns. 3, 4 and 5. However, in the present work, the effect of evaporation must also be considered. Typically, the Tedmon equation [19] is employed for scale thickening under combined growth and evaporation conditions. The Tedmon equation is given as,

$$\frac{dX}{dt} = \frac{k_p}{X} - k_{ev} \tag{6}$$

In this case, to enable an analytical calculation, a simplification of Eq. 6, previously proposed by Pillai et al. [20], was employed in the present work by decoupling the oxide growth contributions due to oxidation ($X_1 = \sqrt{2k_p t}$) and evaporation ($X_2 = k_{ev} t$),

$$X = X_1 + X_2 \tag{7}$$

Plugging Eq. 7 into Eq. 5 and combining with Eq. 4 results in the following equation for N_{Cr}^2, assuming that $N_{Cr,i}$=0 as the critical condition [11],

$$N_{Cr}^2 = \left(\frac{V_{\text{alloy}}}{V_{\text{oxide}}}\right) \sqrt{\frac{\pi t}{D_{Cr}}} \left(\frac{k_p}{2t} + k_{ev}\right) \tag{8}$$

Eq. 8 suggests that N_{Cr}^2 is time dependent which can be expected for non-steady state kinetics. For very short times, using the values given in Table 2 and the calculated values for k_p and k_{ev}, N_{Cr}^2 was calculated to be 5.6 at.% (equivalent to 5.0 wt.%). After about 50h, N_{Cr}^2 was calculated to be 6.4 at.% (equivalent to 5.8 wt.%) and 7.5 at.% (equivalent to 6.8 wt.%) in air+10% H_2O and air+30% H_2O respectively. The corresponding values after 300h were 7.4 at.% (equivalent to 6.7 wt.%) and 10.2 at.% (equivalent to 9.3 wt.%). Based on these calculations, it can be concluded that formation of a chromia scale cannot be

supported if the Cr concentration at the oxide-alloy interface drops below 6.8 wt.% after 50h and 9.3 wt.% after 300h in air+30% H_2O.

Alternatively, an effective parabolic rate constant $k_{p,\,eff}$ based on the total oxide thickness X from Eq. 7 can be calculated and can be employed in Eq. 2 to estimate the time-independent N_{Cr}^2. For an average measured oxide thickness of 0.15 µm after 10h in dry air at 700°C (not shown here), $k_{p,\,eff}$ was calculated to be 5.8x10^{-15} cm^2 s^{-1} for air+10% H_2O and 6.5 x10^{-15} cm^2 s^{-1} for air+30% H_2O. Plugging this value in Eq. 2 results in a value of 5.8 at.% (equivalent to 5.3 wt.%) and 6.3 at.% (equivalent to 6 wt.%) for N_{Cr}^2 in the two environments respectively. Eq. 8 clearly provides more conservative estimates, and these will be employed here.

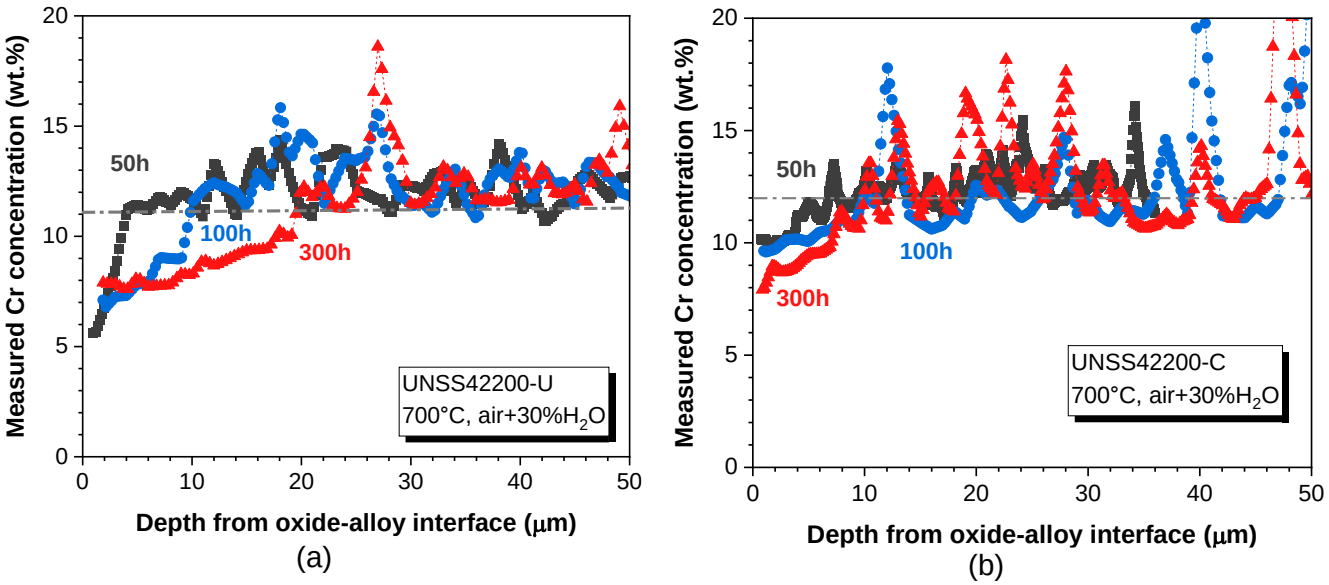

Figure 11: Measured (EDS) Cr concentration profiles for (a) UNSS42200-U and (b) UNSS42200-C after exposure in air+30% H_2O for 50, 100 and 300h at 700°C. The profiles are an average of 3 line profiles. Dashed line indicates the initial Cr content of the alloys.

Figure 11a and b show the measured Cr concentration profiles for UNSS42200-U and UNSS42200-C after exposure in air+30%H_2O for 50, 100 and 300h at 700°C, respectively. For UNSS42200-U, the Cr concentration at the oxide-alloy interface is 5.5 wt.% which is significantly below the much needed 6.8 wt.%. The formation of a chromia scale cannot be supported and that is confirmed by the micrographs in **Figure 2**and the elemental maps in Figure 4. Furthermore, once the duplex Fe-rich oxide structure is established, Cr will predominantly be incorporated into the internal oxide layer and the interface concentration will not vary significantly. In contrast, the interface Cr concentration after 50h in UNSS42200-C is about 10 wt.% and sufficiently high enough to support formation of a chromia scale. The interface concentration does not change considerably even after 100h but drops to 7.9 wt.% after 300h which is below the critical value of 9.3 wt.%. In case of the exposures in air+10%H_2O, the measured interface Cr concentrations (not shown here) were similar to the exposures in air+30%H_2O after 50 and 100h but were about 1 wt.% higher after 300h (8.8 wt.% compared to 7.9 wt.%). The minimum Cr concentration required to sustain chromia scale formation after 300h was 6.7 wt.% in air+10% H_2O and 9.3 wt.% in air+30% H_2O. This result is in very good agreement with the experimental observation of local nodule formation in case of UNSS42200-C after 300h in air+30%H_2O (**Figure 6**). The theoretical calculations can explain the experimental findings and the reasons for the differences in oxidation behavior observed for UNSS42200-U and UNSS42200-C.

The findings for the developmental alloy DA-1 are remarkable. DA-1 showed negligible mass gain with a similar Cr content to alloy UNSS42200-U. The only major difference was the Cu content and a closer look at the oxide layers revealed some interesting insights. The elemental maps shown in **Figure 9** show

the presence of an outer FeCuMn-rich mixed oxide and a Cr-rich oxide underneath. While the specimens were Cu coated to protect the oxide layers and facilitate SEM imaging, this plating also caused the Cu element maps (EDS) to be inconclusive. As such, EDS point analyses (the authors are aware of the uncertainties associated with measuring O by EDS, especially in the alloy) across the oxide scale (**Figure 12**) were performed which did confirm the presence of Cu in the oxide layer with a clear compositional gradient from the gas-oxide to the oxide-alloy interface. The outermost layer is a mixed oxide consisting of FeCuMn which transitions to a MnCr-rich oxide.

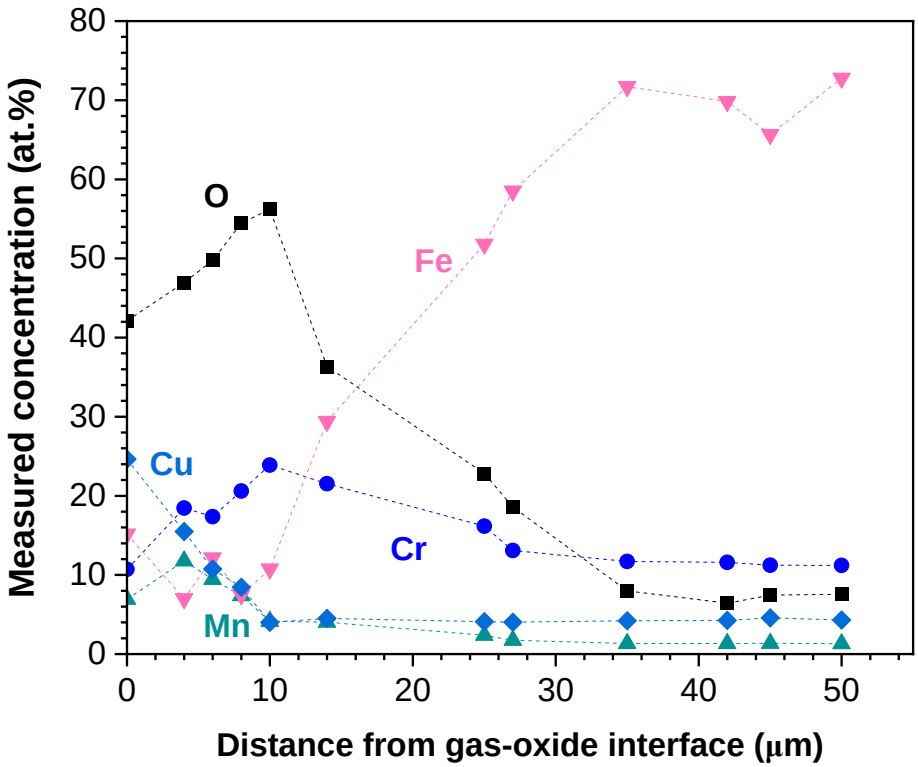

Figure 12: Measured (EDS) concentrations across the oxide layer formed on DA-1 after exposure in air+30% H_2O for 250h at 700°C.

There is limited information in the literature on the combined effects of Cu and Mn on the oxidation behavior of ferritic steels, especially in the O-rich atmospheres employed in the present work. Coatings of CuMn-spinels have been employed on ferritic steel interconnects in solid oxide fuel cells to slow chromia growth and Cr loss due to evaporation [21]. However, the mechanistic understanding for this phenomenon is still unclear. The formation of an FeCu-spinel at the gas-oxide interface is expected based on the thermodynamic stability of Cu- and Fe-oxides. This would decrease the partial pressure of oxygen at the spinel-alloy interface allowing the more stable Cr- oxides to form underneath. Mn is known to diffuse through the FeCr-spinels and Cr-rich oxide scales to result in formation of Mn-rich spinels at the gas-oxide interface [22] both in dry and wet air [23, 24], which was observed to happen for DA-1 in the present work. The results suggest that the FeCuMn-rich oxide layer at the gas-oxide interface is limiting outward Cr-diffusion and thereby also reducing the likelihood of Cr being incorporated in the outer scale. Consequently, any potential volatilization of Cr-rich oxides is prevented and may minimize the Cr loss from the alloy which oxidizes beneath the FeCuMn-spinel. Further investigations are needed to verify these hypotheses intended to explain this discovery of the potential influence of Cu to significantly improve the oxidation resistance of some Fe-Cr-Mn type alloys.

The poor performance of DA-2 compared to DA-1 provides further data to support the role of Cu since the primary difference between alloys DA-1 and DA-2 is the Cu content. Interestingly, although DA-2 has a similar Cr content to UNSS42200-U, the duplex oxide scale formed on DA-2 was significantly thinner. The total oxide thickness (outer + inner layers) was 110±12 μm on UNSS42200-U and 26±4 μm on DA-

2. In the case of duplex Fe-rich oxides on ferritic-martensitic steels, Fe typically diffuses from the alloy to support the growth of the outward growing scale [25]. At the relatively high temperature of 700°C, increased Cr diffusion in the alloy results in a Cr-rich inward-growing scale which inhibits outward Fe diffusion, slows down oxidation kinetics but subsequently causes void formation in the oxide layers [25]. There is clearly a Cr-rich oxide layer at the oxide-alloy interface in the case of DA-2 (**Figure 10**) which is most likely inhibiting outward Fe diffusion and causing the oxide to be more porous than observed for UNSS42200-U. One notable difference between the two alloys is the C content. The higher C content in UNSS42200-U means that the matrix Cr concentration is 9.2 wt.% compared to 10.5 wt.% in the case of DA-2 (based on thermodynamic equilibrium calculations). It is well established that these seemingly minor differences in Cr and C concentrations can play a significant role in the differences in oxidation behavior of ferritic-martensitic steels in water vapor containing environments [26].

CONCLUSIONS

The slightly higher evaporation-induced loss of Cr in the air+30 vol.% H_2O compared to air+10 vol.% H_2O was theoretically shown to be sufficient to result in the breakdown of the chromia scales and formation of Fe-rich oxide nodules on the 12%Cr steel. This predicted result agreed with experimental observations. The role of additional alloying elements in the two UNSS42200 steel variants is a subject of ongoing research. Alloying with Cu in one of the developmental alloys appeared to have a remarkable beneficial effect to improve oxidation resistance in the higher H_2O-containing atmosphere, with negligible mass gain observed even after exposure for 250h in air+30 vol.% H_2O at 700^{o}C.

ACKNOWLEDGEMENTS

K. Hanson performed arc melting and hot rolling of developmental alloys. C. Taylor assisted with heat treatments. G. Garner assisted with the experimental work at ORNL. D. Newberry and T. Lowe are thanked for helping with metallography and microstructural characterization. Access to the SEM was provided by the Nuclear Nonproliferation Division, Oak Ridge National Laboratory. M. Romedenne and S. Bell are thanked for their valuable comments on the paper. This research was sponsored by the U.S. Department of Energy, Office of Vehicle Technologies, Powertrain Materials Core Program. This manuscript has been authored by UT-Battelle, LLC, under contract DE-AC05-00OR22725 with the US Department of Energy (DOE). The US government retains and the publisher, by accepting the article for publication, acknowledges that the US government retains a nonexclusive, paid-up, irrevocable, worldwide license to publish or reproduce the published form of this manuscript, or allow others to do so, for US government purposes. DOE will provide public access to these results of federally sponsored research in accordance with the DOE Public Access Plan (https://www.energy.gov/doe-public-access-plan).

REFERENCES

1. Stefan, E., et al., *Materials challenges in hydrogen-fuelled gas turbines.* International Materials Reviews, 2021. **67(5)**: p. 1-26.
2. Thornton, M., M. Ratcliff, and K. Kelly, *Off-Road Vehicle Decarbonization and Energy Systems Integration: R&D Gaps and Opportunities*. 2022: United States. p. Medium: ED; Size: 24 p.
3. Stępień, Z., *A Comprehensive Overview of Hydrogen-Fueled Internal Combustion Engines: Achievements and Future Challenges.* Energies, 2021. **14**(20): p. 6504.
4. Pierce, D., et al., *High temperature materials for heavy duty diesel engines: Historical and future trends.* Progress in Materials Science, 2019. **103**: p. 109-179.
5. Pint, B.A., *Invited Review Paper in Commemoration of Over 50 Years of Oxidation of Metals: Addressing the Role of Water Vapor on Long-Term Stainless Steel Oxidation Behavior.* Oxidation of Metals, 2021. **95**(5): p. 335-357.
6. Pillai, R. and B.A. Pint, *The Role of Oxidation Resistance in High Temperature Alloy Selection for a Future with Green Hydrogen.* JOM, 2021. **73**(12): p. 3988-3997.
7. Young, D.J. and B.A. Pint, *Chromium volatilization rates from Cr_2O_3 scales into flowing gases containing water vapor.* Oxidation of Metals, 2006. **66**(3-4): p. 137-153.
8. Maris-Sida, M.C., G.H. Meier, and F.S. Pettit, *Some water vapor effects during the oxidation of alloys that are alpha-Al(2)O(3) formers.* Metallurgical and Materials Transactions a-Physical Metallurgy and Materials Science, 2003. **34a**(11): p. 2609-2619.
9. Gingrich, E., et al., *Evaluation of High-Temperature Martensitic Steels for Heavy-Duty Diesel Piston Applications.* 2022. **2022**.
10. Pierce, D.T., et al., *Evaluation of thermal processing and properties of 422 martensitic stainless steel for replacement of 4140 steel in diesel engine pistons q.* Materials & Design, 2022. **214**.
11. Wagner, C., *Theoretical Analysis of the Diffusion Processes Determining the Oxidation Rate of Alloys.* Journal of the Electrochemical Society, 1952. **99**(10): p. 369-380.
12. Williams, P.I. and R.G. Faulkner, *Chemical Volume Diffusion-Coefficients for Stainless-Steel Corrosion Studies.* Journal of Materials Science, 1987. **22**(10): p. 3537-3542.
13. Tokei, Z., et al., *Diffusion of chromium in ferritic and austenitic 9-20 wt-% chromium steels.* Materials Science and Technology, 2000. **16**(10): p. 1129-1138.
14. Swisher, J.H. and Turkdoga.Et, *Solubility Permeability and Diffusivity of Oxygen in Solid Iron.* Transactions of the Metallurgical Society of Aime, 1967. **239**(4): p. 426-431.
15. Rapp, R.A., *The Transition from Internal to External Oxidation and the Formation of Interruption Bands in Silver-Indium Alloys.* Acta Metallurgica, 1961. **9**(8): p. 730-741.
16. Asteman, H., et al., *Indication of chromium oxide hydroxide evaporation during oxidation of 304L at 873 K in the presence of 10% water vapor.* Oxidation of Metals, 1999. **52**(1-2): p. 95-111.
17. Romedenne, M., et al., *Oxidation Lifetime Modeling of 625 and 120 Foils After Long-term Exposure in Flowing Air + 10% H_2O at 700 and 800 °C.* Oxidation of Metals, 2022. **98**(3): p. 305-324.
18. Young, D.J., *High temperature oxidation and corrosion of metals*. 2008, Oxford: Elsevier.
19. Tedmon, C.S., *The Effect of Oxide Volatilization on the Oxidation Kinetics of Cr and Fe-Cr Alloys.* Journal of the Electrochemical Society, 1966. **113**(8): p. 3.
20. Pillai, R., S. Dryepondt, and B.A. Pint. *High Temperature Oxidation Lifetime Modeling of Thin-Walled Components*. in *ASME Turbo Expo 2019: Turbomachinery Technical Conference and Exposition*. 2019.
21. Acharya, N., et al., *Highly dense Mn3O4 and CuMn2O4 spinels as efficient protective coatings on solid oxide fuel cell interconnect and their chromium diffusion studies.* Journal of Alloys and Compounds, 2022. **918**: p. 165377.

22. Lobnig, R.E., et al., *Diffusion of Cations in Chromia Layers Grown on Iron-Base Alloys.* Oxidation of Metals, 1992. **37**(1-2): p. 81-93.
23. Romedenne, M., et al., *Effect of Water Vapor on Lifetime of 625 and 120 Foils During Oxidation Between 650 and 800 °C.* Oxidation of Metals, 2021. **96**(5): p. 589-612.
24. Romedenne, M., et al., *Revealing the elusive role of water vapor in the oxidation behavior of a Mn-Si containing NiCr alloy at 950 °C.* Corrosion Science, 2023. **221**: p. 111348.
25. Zurek, J., et al., *Anomalous temperature dependence of oxidation kinetics during steam oxidation of ferritic steels in the temperature range 550-650 degrees C.* Corrosion Science, 2004. **46**(9): p. 2301-2317.
26. Ennis, P.J. and W.J. Quadakkers, *Mechanisms of steam oxidation in high strength martensitic steels.* International Journal of Pressure Vessels and Piping, 2007. **84**(1-2): p. 75-81.